Journal of Magnetic Resonance 302 (2019) 43–49

Contents lists available at ScienceDirect

Journal of Magnetic Resonance

journal homepage: www.elsevier.com/locate/jmr

Improved waveguide coupling for 1.3 mm MAS DNP probes at 263 GHz

Armin Purea [a], Christian Reiter [a], Alexandros I. Dimitriadis [b], Emile de Rijk [b], Fabien Aussenac [c], Ivan Sergeyev [d], Melanie Rosay [d], Frank Engelke [a,*]

[a] Bruker Biospin GmbH, Rheinstetten, Germany
[b] Swissto12, Renens, Switzerland
[c] Bruker France S.A.S., Wissembourg, France
[d] Bruker Biospin, Billerica, USA

ARTICLE INFO

Article history:
Received 19 February 2019
Revised 26 March 2019
Accepted 27 March 2019
Available online 28 March 2019

Keywords:
Dynamic nuclear polarization
DNP
Sub-THz microwave fields
Simulation of electromagnetic fields
Nuclear magnetic resonance
Solid-state NMR instrumentation
Magic angle spinning

ABSTRACT

We consider the geometry of a radially irradiated microwave beam in MAS DNP NMR probes and its impact on DNP enhancement. Two related characteristic features are found to be relevant: (i) the focus of the microwave beam on the DNP MAS sample and (ii) the microwave magnetic field magnitude in the sample. We present a waveguide coupler setup that enables us to significantly improve beam focus and field magnitude in 1.3 mm MAS DNP probes at a microwave frequency of 263 GHz, which results in an increase of the DNP enhancement by a factor of 2 compared to previous standard hardware setups. We discuss the implications of improved coupling and its potential to enable cutting-edge applications, such as pulsed high-field DNP and the use of low-power solid-state microwave sources.

© 2019 Elsevier Inc. All rights reserved.

1. Introduction

The increasing popularity of DNP MAS NMR of solids samples during the past decade has much benefitted from theoretical progress (DNP under MAS [1–9], DNP without MAS [10–18]), optimizing biradicals for MAS DNP [19–33], and continuous advances of the hardware elements in MAS DNP probes [34–74]. Part of these improvements concentrate on a detailed understanding, optimization, and better control of how a polarized microwave beam exiting a waveguide with its aperture close to the DNP MAS sample propagates through the NMR rf coil, the MAS rotor walls and the sample [34–37,46–71] – in short, how the microwave beam couples to the sample. This is not only reflected in the abundant scientific literature, but also in the patent literature [51,54,56–60,64,65,70], and is an indicator for the active research and development in the field of microwave instrumentation for MAS DNP NMR. Specifically for the MAS geometry the microwave beam coupling has been studied for the case of axial irradiation (*i.e.*, along the rotor axis or cylindrical sample axis, [52,56,61,63–66]) and for the case of radial irradiation (*i.e.*, perpendicular to the MAS rotor axis, [34,46,48,49,59,62,69–71]). In the present paper we introduce a novel microwave beam coupler design [70,71] for radially irradiating the DNP sample in 1.3 mm MAS DNP probes, which enables us to increase the continuous wave (CW) microwave magnetic field magnitudes in the sample volume by about a factor 3, with the result that the DNP enhancement factor (ratio of signal amplitudes with microwave on and off) also increases by a factor of approximately 2.

2. Simulation and experimental results

Fig. 1 sketches the geometry of the waveguide coupler and the magnetic field magnitudes of the transmitted beam. In Fig. 1a and b the microwave magnetic fields are shown in the central radial and axial planes for the standard design of Bruker 1.3 mm MAS DNP probes. Fig. 1c and d refer to these microwave fields in our novel improved design, whose geometric layout is shown in Fig. 1e. The incident microwave beam at 263 GHz enters from the right side through a planar/convex lens with focus on the right entrance of the small, smooth-wall waveguide. The waveguide aperture on the left end is in close proximity (1 mm) to the solenoidal rf coil (tuned to 400 MHz and to X nucleus frequencies). On the back-end a mirror made of gold foil is placed to reflect the beam after it has passed through the coil, the rotor and the sample. The 2 mm id. waveguide, the rf coil leads, the rf coil itself and

* Corresponding author.
E-mail address: frank.engelke@bruker.com (F. Engelke).

https://doi.org/10.1016/j.jmr.2019.03.009
1090-7807/© 2019 Elsevier Inc. All rights reserved.

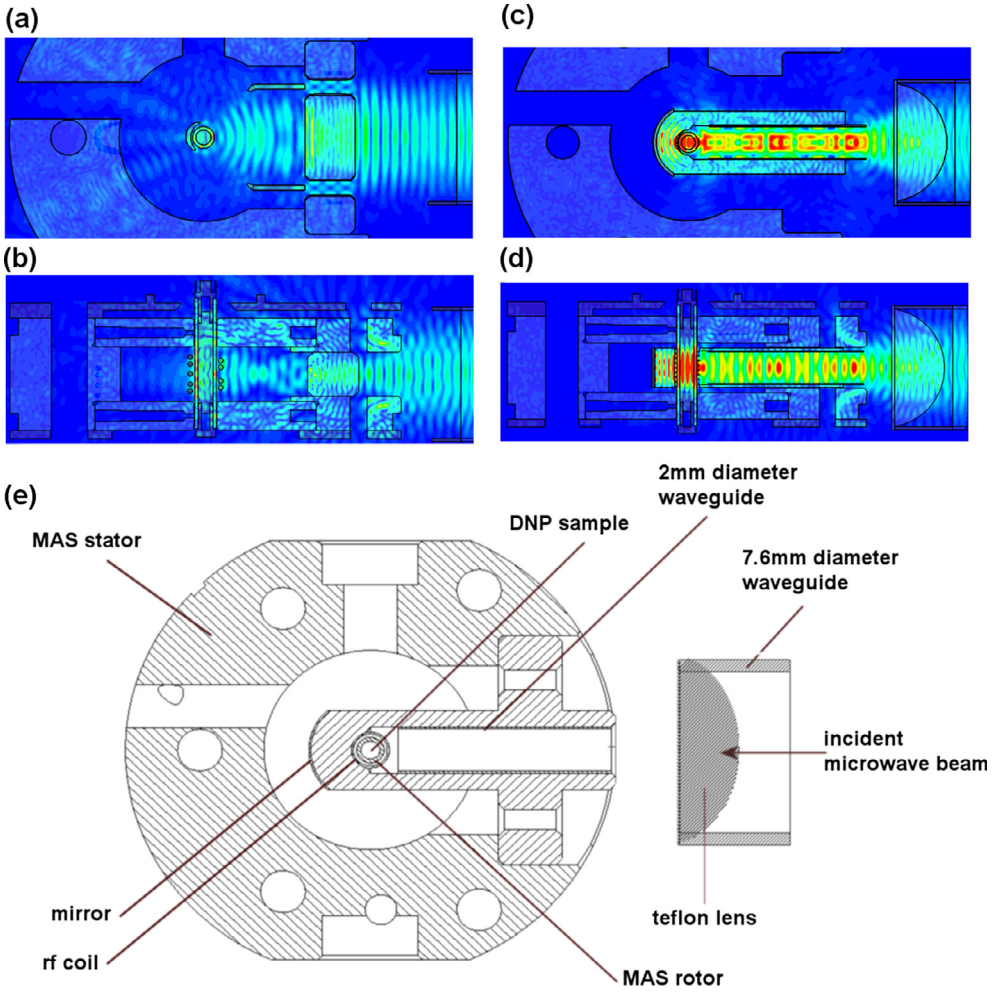

Fig. 1. Simulated microwave magnetic field magnitudes $|B_1|$ (snapshots) of the microwave beam propagating through the 1.3 mm MAS DNP system. (a) Radial and (b) axial cross section of the system with teflon lens only ("standard system"). (c) Radial and (d) axial cross section of the system with lens and short 2 mm inner diameter waveguide section ("optimized system"). (e) Geometry of the optimized design. Color coding: red – high amplitude, yellow and green – medium amplitudes, blue – low amplitude of the microwave magnetic field. (For interpretation of the references to colour in this figure legend, the reader is referred to the web version of this article.)

the mirror are mounted into a monolithic block made of dielectric material, *e.g.*, of Shapal M (FiberOptic P. + P. AG, Spreitenbach, Switzerland) or quartz glass (LightFab GmbH, Aachen, Germany). The monolithic block contains one axial bore to house the rf coil and the MAS rotor, and one radial bore for the 2 mm id. waveguide. The gold-plated mirror is on the rear outer surface.

The numerical field simulations were conducted using CST Microwave Studio 2017 (CST, Darmstadt, Germany). The simulations of all microwave field components (electric and magnetic) at 263 GHz were performed using the time-domain solver with a spatial resolution (mesh cell size) between 22 μm and 126 μm. The mesh was varied to account for the slower wave propagation in dielectric material, which leads to shorter wavelengths. The total number of hexagonal mesh cells in 3D space amounted to 45×10^6. A broadband excitation pulse of approximately 10 ps length with Gaussian profile in both time and space was emitted from a waveguide port at the end of the waveguide stub. The simulation was run until the energy within the boundaries has decayed to −30 dB. A frequency field monitor at 263 GHz was used to evaluate the B_1 field profile.

In Fig. 1c and d magnetic field amplitudes of the incident microwave beam are shown in the central radial and axial planes of the MAS rotor and rf coil. At the exit of the corrugated waveguide (right side of Fig. 1c and d) the HE_{11} beam (linearly polarized with Gaussian intensity profile) propagates through a convex-planar lens made of PTFE, which focuses the beam onto the 2 mm id. waveguide entrance side. Simulation of this coupling scheme showed that 76% of the input power is coupled into the small waveguide. Inside the small waveguide the beam is primarily propagating as TE_{11} (93%) and TM_{11}(4%). The remaining 3% can be attributed to higher-order modes and ohmic loss in the metal (see Supplementary Information). On the left side the compressed beam leaving the small waveguide further propagates through the NMR rf solenoidal coil (id. ca. 1.6 mm, wire diameter 0.13 mm, pitch 0.3 mm), through the rotor wall (zirconia, real part of dielectric constant 33, determined experimentally at 140–220 GHz and 500–750 GHz using the Material Characterization Kit by Swissto12), through the DNP sample (dielectric constant assumed to be 3.5 [34]) inside the rotor (id. 0.9 mm), through the rear rotor wall, the material of the block assembly (Shapal M, dielectric constant equal to 7 [72]) to finally get reflected at the mirror, generating a scattered beam propagating backwards through the whole setup again. The presence of the mirror accounts for about 10% field amplitude increase. As the color scale of Fig. 1a–d shows (blue color: low field amplitudes, red color: high field amplitudes), the waveguide coupler leads to a significantly higher magnetic field amplitude inside the rotor in the sample volume. We also recognize that the beam focus caused by the small waveguide leads to

higher microwave field amplitudes close to the rf coil and inside the rotor wall.

Experimentally, the close proximity of the small-diameter waveguide or the mirror relative to the sample do not cause any noticable acoustic ringing. As far as shimming is concerned, an FWHM of 6 Hz for the ^{13}C NMR lines of adamantane at room temperature could be achieved.

In order to quantify the microwave magnetic field magnitudes, a spatial average over the whole sample volume inside the 1.3 mm MAS rotor was calculated. Since the power of the simulated incident microwave beam is known (it has been set to P = 0.5 W) the averaged microwave magnetic field magnitudes B_1 can be normalized to the input power. This way, the (average) microwave magnetic field *efficiency* $B_1/P^{1/2}$ can be determined.

The microwave field efficiencies thus obtained are listed in Table 1 for comparison, given in $B_1/P^{1/2}$ (in $\mu T/W^{1/2}$), or equivalently in frequency units, $\gamma_e B_1/(2\pi P^{1/2})$ (in $MHz/W^{1/2}$). The quantity γ_e denotes the gyromagnetic ratio for the electron spin. The listed configurations include a standard Bruker 3.2 mm MAS DNP probe at 400 MHz/263 GHz, a standard Bruker 1.3 mm MAS DNP probe (*i.e.*, without the 2 mm id. waveguide coupler), and our present novel design (1.3 mm MAS DNP probe with 2 mm id. waveguide coupler, Fig. 1). With the latter an average microwave field efficiency of 1.8 $MHz/W^{1/2}$ was achieved, about a factor of ca. 3 higher than the other DNP NMR probe designs. The peak field value in the sample was 5.9 $MHz/W^{1/2}$ (see Supplementary Information). It is interesting to compare the efficiency values achieved for MAS DNP probes with typical efficiency values as known from EPR probes – two examples are given in Table 1 For a Bruker EPR probe at 263 GHz with a Fabry-Perot type cavity for 5 mm EPR samples, one achieves a microwave field efficiency of ca. 6 $MHz/W^{1/2}$, while for a fundamental mode (TE_{011}) cavity, which has a higher Q factor and a much smaller sample volume (0.3 mm capillary samples), one achieves 36 $MHz/W^{1/2}$.

In order to confirm the improvement of the microwave magnetic field magnitude in our proposed design, we performed ^1H–^{13}C CPMAS DNP experiments measuring ^1H DNP enhancement factors of a sample of frozen (ca. 100 K) water/glycerol/proline/AMUPol spinning at an MAS rates of 10 and 40 kHz with the optimized 1.3 mm MAS DNP probe and MAS 10 kHz with the previous standard probe. All experiments were performed on a 400 MHz/263 GHz DNP NMR system with a Bruker/CPI gyrotron as microwave source, except one single measurement at an incident microwave power of 0.25 W, where a solid-state source (VDI) has been used [73]. The incident microwave power has been calibrated and varied by changing the gyrotron collector beam current between 0 and 150 mA (corresponding to power levels between 0 and 8.2 W at the DNP sample). The experimental ^1H DNP enhancement results are shown in Fig. 2a. For an MAS frequency of 10 kHz at low microwave power levels of 2 W we find a factor of about 2 of improved DNP enhancement, at higher power levels (8 W) the improvement is less, but still 15%. This finding clearly correlates with the magnetic microwave field magnitudes obtained by simulations. When spinning at 40 kHz the DNP enhancements with the optimized probe are about 20% lower as compared to spinning at 10 kHz with the same probe. It is also visible that with the optimized probe the saturation is achieved at lower power levels as compared to the nonoptimized one. The temperature of the sample has been measured using the temperature dependence of ^{79}Br T_1 in a separate KBr sample [74]. In Fig. 2b the dependence of the sample temperature on microwave power and MAS rate is plotted. For MAS 10 kHz (two lower curves) the temperature increase can be mainly attributed to the incident microwave power. At MAS rates of 40 kHz (upper curve) a second mechanism comes into play – the frictional heating of the rotor and sample when spinning fast – thus the temperatures for that case are higher by about 15 K.

Table 1
Microwave field efficiencies (magnetic field amplitude B_1 divided by the square root of incident power) for a variety of MAS DNP configurations and compared to typical EPR probe configurations at 263 GHz.

Configuration	$B_1/P^{1/2}$ ($\mu T/W^{1/2}$)	$\gamma_e B_1/(2\pi P^{1/2})$ ($MHz/W^{1/2}$)
3.2 mm MAS DNP standard	20	0.56
1.3 mm MAS DNP standard	19	0.53
1.3 mm MAS DNP optimized	66	1.8
EPR 263 GHz, Fabry-Perot $TEM_{10\ 0\ 0.6}$ cavity for 5 mm EPR samples	213	6
EPR 263 GHz TE_{011} cavity for 0.3 mm capillary EPR samples	1270	36

The simulation results introduced so far leave one question open: does the increase of B_1 field magnitudes as suggested by Fig. 1c and d originate from the much improved focusing of the microwave beam through the small waveguide being better adapted to the small sample region in 1.3 mm MAS rotors or is it caused by some specific resonant features provided by the rf coil, the 1.3 mm MAS rotor made of zirconia, the frozen DNP NMR sample, and the block assembly made of dielectric material (Shapal M). At 263 GHz microwave frequency the free-space wavelength is about 1.1 mm; inside zirconia (dielectric constant 33) the wavelength is compressed to ca. 0.2 mm, while in the sample (dielectric constant 3.5) it is 0.6 mm. The wave magnitude maxima (maxima and minima in amplitude) can be clearly seen in Fig. 1d inside the MAS rotor. Principally, there is evidence that, for example, the MAS rotor and the sample introduce features of a dielectric resonator, albeit not perfectly tuned to the specific frequency of 263 GHz. The question is whether the improvement of $B_1/P^{1/2}$ (from 0.5 $MHz/W^{1/2}$ to 1.8 $MHz/W^{1/2}$ in Table 1) is dominated by such resonant features or rather alone by the improved focus of the microwave field.

Extending our previous simulation methodology of monitoring electromagnetic fields at a certain frequency, the resonant behavior of a certain design can be studied by monitoring the field at successive points in time. Thus, the propagation of the same short, broadband microwave pulse through the structure of interest is obtained. Such time domain monitoring was carried out for the 3.2 mm standard configuration as well as the 1.3 mm optimized configuration with small waveguide coupler.

The same simulation parameters as described above were used, with the only exception that frequency monitoring was replaced by time monitoring. Time sampling was chosen at time steps of 0.5 ps for the time between 60 ps and 500 ps. At 263 GHz this corresponds to about 7.6 points per cycle and an acquisition window of 115 cycles. For each point in time, the simulated electric field magnitude was averaged over the sample volume. The resulting decay pattern over time, normalized to its respective maximum during the pulse, is illustrated in Fig. 3 for the standard 3.2 mm MAS DNP probe (red curve) and the 1.3 mm MAS DNP probe with small waveguide coupler (blue curve). The irregular features of both decay curves originate from multiple scattering (diffractions and reflections) of the initially confined beam by the metallic and dielectric structures (rf coil, mirror, rotor walls, stator walls, the structure of the coil block assembly). The overall behavior, however, is clearly visible: the field magnitudes decay on the order of 0.15 ns.

More importantly, the decays of both field curves – for the standard setup and for the setup with the small waveguide coupler – are very similar as far as the characteristic decay time constants (ca. 0.15 ns) are concerned. From the decay time τ_E of ca. 0.15 ns we may conclude an "apparent or phenomenological Q factor" on the order of

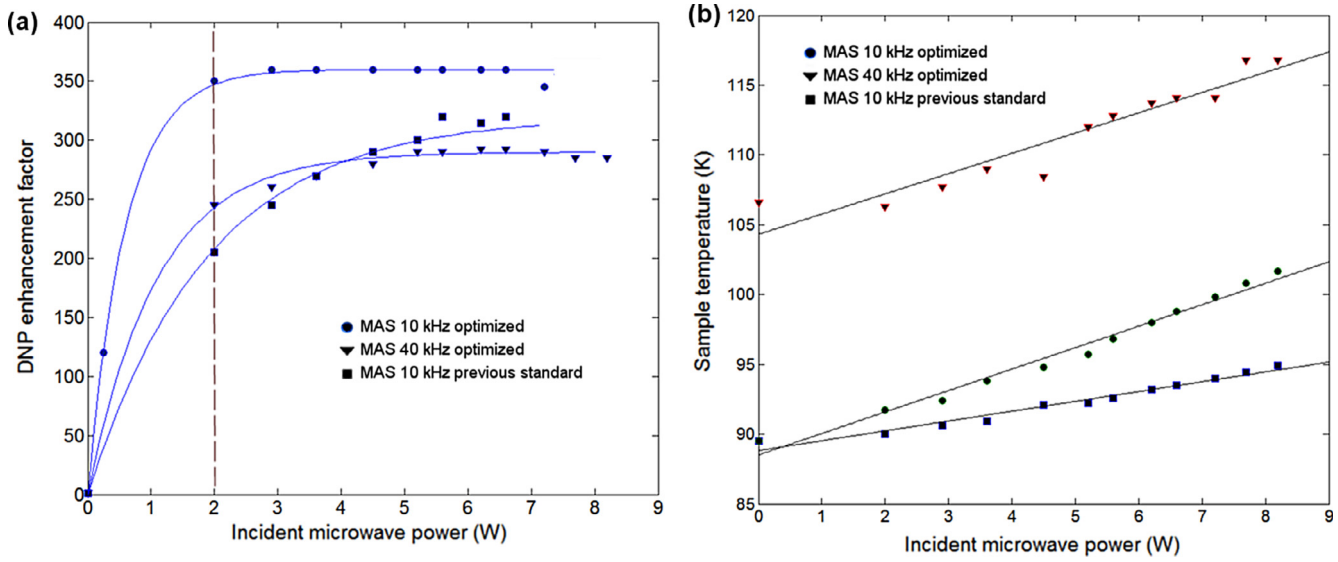

Fig. 2. (a) ^{1}H MAS DNP enhancement factor vs. incident microwave power of 0.25 M ^{13}C-^{15}N proline with 10 mM AMUPol in glycerol-d8/D_2O/H_2O (60/30/10 vol ratio) for MAS frequencies of 10 and 40 kHz for the optimized design and MAS 10 kHz for the previous standard design. The data point at 0.25 W power has been taken with a solid-state microwave source [73], see the Discussion section, while all other data points at higher power levels were obtained with a gyrotron source. The full curves were obtained by fitting an exponential function to the data and only serve to guide the eye. (b) Sample temperature vs. incident microwave power for MAS frequencies of 10 and 40 kHz for the optimized design and 10 kHz for the previous standard design.

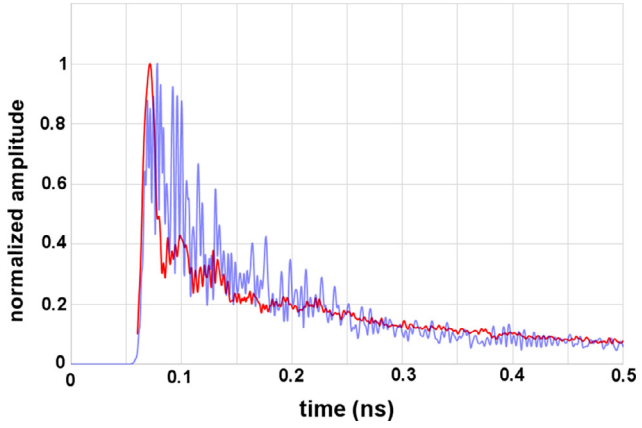

Fig. 3. Simulated electric microwave field magnitude over time during a short beam pulse propagating through the DNP MAS sample volume. Red curve – 3.2 mm MAS DNP probe with lens and mirror (blue curve – 1.3 mm MAS DNP setup with lens, mirror and short 2 mm waveguide. (For interpretation of the references to colour in this figure legend, the reader is referred to the web version of this article.)

$$Q_{E2} = \frac{1}{2}\pi f_0 \tau_E \quad (1)$$

which for f_0 = 263 GHz and $\tau_E \approx 0.15$ ns yield the value $Q_{E2} \approx 60$. The value of τ_E (or of Q_{E2}) is about the same for both cases, hence the resonant features are not affected by adding the small waveguide coupler. More details on phenomenological *Q* factors in DNP MAS microwave field irradiation will be published elsewhere [75]. With the findings reported in this paper we have to conclude that the higher magnetic field magnitudes are *not* caused by any change of the apparent *Q* factor, but it is rather the improvement in beam focusing that yields higher microwave fields.

3. Discussion

The results obtained with the new design at 263 GHz are beneficial for current CW DNP experiments. We have shown that the increased efficiency leads to higher DNP enhancements compared to previous existing designs when abundant power is available. When power is limited and the DNP enhancement vs. B_1^2 is in the linear regime, the relative increase is even more important. The proposed setup therefore paves the way to the use of lower-power microwave sources like klystrons or even solid-state sources [76] while still obtaining reasonable DNP enhancements that are sufficient for certain DNP applications. Since the proportionality $P \propto B_1^2$ holds between the power P and the magnetic field B_1, an improvement by a factor of 3 for B_1 efficiency translates in almost a factor of 10 in savings of microwave power P for the same DNP enhancement – a worthwhile goal to follow for solid-state NMR DNP systems operating at 263 GHz.

A brief instructive example is shown in Fig. 4. The improved 1.3 mm MAS DNP probe described above was used with a 250 mW VDI source and a DNP enhancement of more than 100 was obtained in that low power range. More details will be described in a publication elsewhere [73].

The prospect to use lower-power microwave sources, *e.g.*, proposed for low-temperature (25 K) DNP at 9.4 T by Thurber et al. [76] now appears to be feasible also at higher cryogenic temperature (e.g., 100 K) including small-diameter MAS. Besides of the technical aspect, the resulting possibilities also encompass the economic aspects (price and footprint) of lower-power microwave sources, notably klystrons and solid-state sources.

Considering the achievable microwave B_1 amplitude values from our simulations, especially electron Rabi (nutation) frequencies in the MHz range attainable at 263 GHz/9.4 T (corresponding to 400 MHz proton frequency), another aspect worth discussing is to what extent such a design may be useful for *pulsed, swept or time-domain DNP NMR experiments* [46,77–88], for instance, to decouple the hyperfine interaction [46] or to perform NOVEL-type experiments [77–81]. From the values given in Table 1 it becomes clear that the microwave magnetic field amplitudes, although reasonably high for electron decoupling [46], are still far below the values that would allow NOVEL-type experiments at 9.4 T.

Among the various mechanisms for DNP MAS in solids – DNP based on the cross effect (CE), the solid effect (SE) or the

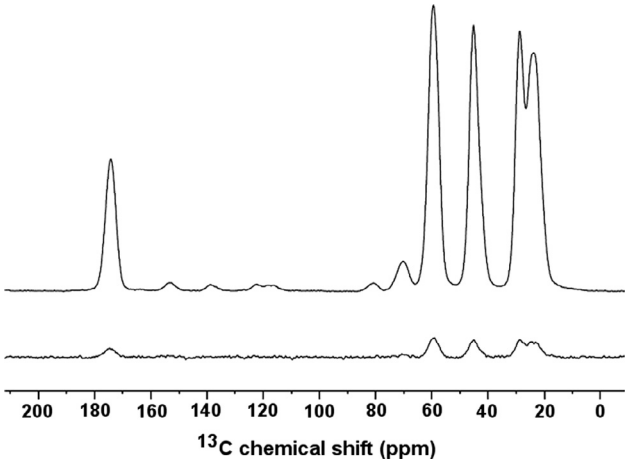

Fig. 4. ^{13}C CP-MAS spectra of 0.25 M ^{13}C-^{15}N proline with 10 mM AMUPol in glycerol-d8/D_2O/H_2O (60/30/10 vol ratio) with microwave irradiation (top spectrum, 8 scans) and without microwave irradiation (bottom spectrum, 64 scans). Sample volume inside NMR coil 1.7 μl. Spinning frequency: 10 kHz, sample temperature: 98 K, 2 dummy scans, 10 s recycle delay. Spectra were obtained at a power level of 250 mW with solid-state source (VDI, Charlottesville, Virginia) operating at 263 GHz (upper spectrum), leading to a DNP enhancement of approximately 120 with the 1.3 mm MAS DNP optimized probe relative to the microwaves off (lower spectrum).

solids-Overhauser effect [21,89–91] – SE DNP needs more microwave power as compared to CE DNP and Overhauser DNP [89]. Thus the improvement of the microwave efficiency of our 1.3 mm MAS DNP probe may well turn out as beneficial for DNP applications utilizing SE DNP.

The DNP enhancements reported in the present paper are by far not the highest enhancements achieved. For example, Kubicki et al. [92] measured ^{1}H enhancement factors as high as 515 for TCE/TEKPol samples with small sub-mm sapphire particles embedded in the sample, where the volume filling factor of the sapphire particles amounted to 65%, leaving 35% for the DNP active sample. This effect of enlarging the DNP enhancement factor was attributed to a redistribution and increase of the local magnetic microwave fields originating from multiple near-field scattering caused by the dielectric sapphire particles. To our best knowledge, the details of this effect are not yet well enough understood but certainly deserve further studies. Although the DNP enhancement factor achievable is impressive, one loses active sample volume by the presence of the particles, in the above example it is 65%.

Finally, all results reported here so far were obtained for 263 GHz. Since there is a lot of ongoing DNP activity at higher electron Larmor frequencies such as 395, 527 and even 593 GHz, it is worth considering to what extent the encouraging results introduced in the present paper for MAS 1.3 mm probes may benefit higher microwave frequencies by redesigning the small waveguide coupler. On somewhat related terms, the question might be asked, whether the technology presented here can also be applied to larger MAS diameters, e.g., MAS 1.9 mm. A preliminary simulation study revealed the following principal behavior for microwave magnetic field magnitudes B_1: with increasing MAS diameter (from 1.3 to 1.9 mm) at 263 GHz the improvement in B_1 drops from a factor ≈3 to ≈2. At 1.3 mm and 527 GHz, the B_1 field magnitude improvement is equal to ca. 1.5, while for 1.9 mm and 527 GHz, it is about 1.2. Thus with the current waveguide coupler geometry, the larger the MAS diameter and the higher the microwave frequency, the lower the gain in B_1 magnitude. We are currently working on a systematic assessment of the relation between MAS diameter, microwave frequency, and B_1 field.

Acknowledgements

The authors are indebted to Marek Pruski and his group at Ames Laboratory, and Anne Lesage and her team at ENS Lyon, for validating the novel design by experiments.

The work presented here was supported by the European Commission within the Eurostars Program, Project E! 9647–DNP-HOPE.

Appendix A. Supplementary material

Supplementary data to this article can be found online at https://doi.org/10.1016/j.jmr.2019.03.009.

References

[1] K.R. Thurber, R. Tycko, Theory for cross effect dynamic nuclear polarization under magic angle spinning in solid state nuclear magnetic resonance: the importance of level crossings, J. Chem. Phys. 137 (2012) 084508.
[2] K.R. Thurber, R. Tycko, Perturbation of nuclear spin polarization in solid state NMR of nitroxide-doped samples by magic-angle spinning without microwaves, J. Chem. Phys. 140 (2014) 184201.
[3] K.R. Thurber, R. Tycko, On mechanisms of dynamic nuclear polarization in solids, Isr. J. Chem. 54 (2014) 39–46.
[4] B. Corzilius, Theory of solid effect and cross effect dynamic nuclear polarization with half-integer high-spin metal polarizing agents in rotating solids, Phys. Chem. Chem. Phys. 18 (2016) 27190–27204.
[5] F. Mentink-Vigier, S. Vega, G. de Paepe, Fast and accurate MAS-DNP simulations of large spin ensembles, Phys. Chem. Chem. Phys. 19 (2017) 3506–3522.
[6] F.A. Perras, A. Sadow, M. Pruski, In silico design of DNP polarizing agents: can current dinitroxides be improved?, Chem Phys. Chem. 18 (2017) 2279–2287.
[7] D. Mance, P. Gast, M. Huber, M. Baldus, K.L. Ivanov, The magnetic field dependence of cross-effect dynamic nuclear polarization under magic angle spinning, J. Chem. Phys. 142 (2015) 234201.
[8] F. Mentink-Vigier, U. Akbey, Y. Hovav, S. Vega, H. Oschkinat, A. Feintuch, Fast passage dynamic nuclear polarization on rotating solids, J. Magn. Reson. 224 (2012) 13–21.
[9] A. Equbal, A. Leavesley, S.K. Jain, S. Han, Cross-effect dynamic nuclear polarization explained: polarization, depolarization, and oversaturation, J. Phys. Chem. Letters 10 (2019) 548–558.
[10] Y. Hoav, A. Feintuch, S. Vega, D. Goldfarb, Dynamic nuclear polarization using frequency modulation at 3.34 T, J. Magn. Reson. 238 (2014) 94–105.
[11] D. Wisniewski, A. Karabanov, I. Lesanovsky, W. Köckenberger, Solid effect DNP polarization dynamics in a system of many spins, J. Magn. Reson. 264 (2016) 30–38.
[12] A. Karabanov, G. Kwiatkowski, C.U. Perotto, D. Wisniewski, J. McMaster, I. Lesanovsky, W. Köckenberger, Dynamic nuclear polarisation by thermal mixing: quantum theory and macroscopic simulations, Phys. Chem. Chem. Phys. 18 (2016) 30093–30104.
[13] A. Karabanov, D. Wisniewski, I. Lesanovsky, W. Köckenberger, DNP as kinetically constrained diffusion, Phys. Rev. Lett. 115 (2015) 020404.
[14] A. Karabanov, A. van der Drift, L.J. Edwards, I. Kuprov, W. Köckenberger, Quantum mechanical simulation of solid effect dynamic nuclear polarisation using Krylov-Bogolyubov time avaraging and a restricted state-space, Phys. Chem. Chem. Phys. 14 (2012) 2658–2668.
[15] A. Karabanov, G. Kwiatkowski, W. Köckenberger, Quantum mechanical simulation of cross effect DNP using Krylov-Bogolyubov averaging, Appl. Magn. Reson. 43 (2012) 43–58.
[16] D. Shimon, A. Feintuch, D. Goldfarb, S. Vega, Static ^{1}H dynamic nuclear polarization with the biradical TOTAPOL: a transition between the solid effect and the cross effect, Phys. Chem. Chem. Phys. 16 (2014) 6687–6699.
[17] D. Banerjee, D. Shimon, A. Feintuch, S. Vega, D. Goldfarb, The interplay between the solid effect and the cross effect mechanisms in solid state ^{13}C-DNP at 95 GHz using trityl radicals, J. Magn. Reson. 230 (2013) 212–219.
[18] Y. Hovav, A. Feintuch, S. Vega, Theoretical aspects of dynamic nuclear polarization in the solid state – the solid effect, J. Magn. Reson. 207 (2010) 176–189.
[19] C. Song, K.-N. Hu, C.-G. Joo, T.M. Swager, R.G. Griffin, TOTAPOL: a biradical polarizing agent for dynamic nuclear polarization experiments in aqueous media, J. Am. Chem. Soc. 128 (2006) 11385–11390.
[20] Y. Matsuki, T. Maly, O. Ouari, H. Karoui, F. Le Moigne, E. Rizzato, S. Lyubenova, J. Herzfeld, T. Prisner, P. Tordo, R.G. Griffin, Dynamic nuclear polarization using a rigid biradical, Angew. Chem. Int. Ed. 48 (2009) 4996–5000.
[21] E.L. Dane, B. Corzilius, E. Rizzato, P. Stocker, T. Maly, A.A. Smith, R.G. Griffin, O. Ouari, P. Tordo, T.M. Swager, Rigid orthogonal bis-TEMPO biradicals with improved solubility for dynamic nuclear polarization, J. Org. Chem. 77 (2012) 1789–1797.
[22] A.J. Rossini, A. Zagdoun, M. Lelli, J. Canivet, S. Aguado, O. Ouari, P. Tordo, M. Rosay, W.E. Maas, C. Coperet, D. Farrusseng, L. Emsley, A. Lesage, Dynamic nuclear polarization enhanced solid state NMR spectroscopy of functionalized metal-organic frameworks, Angew. Chem., Int. Ed. 51 (2012) 123–127.

[23] A. Zagdoun, G. Casano, O. Ouari, G. Lapadula, A.J. Rossini, M. Lelli, M. Baffert, D. Gajan, L. Veyre, W.E. Maas, M. Rosay, R.T. Weber, C. Thieuleux, C. Copéret, A. Lesage, P. Tordo, L. Emsley, A slowly relaxing rigid biradical for efficient dynamic nuclear polarization surface- enhanced NMR spectroscopy: expeditious characterization of functional group manipulation in hybrid materials, J. Am. Chem. Soc. 134 (2012) 2284–2291.
[24] C. Sauvee, M. Rosay, G. Casano, F. Aussenac, R.T. Weber, O. Ouari, P. Tordo, Highly efficient water-soluble polarizing agents for dynamic nuclear polarization at high frequency, Angew. Chem. 125 (2013) 11058–11061.
[25] A. Zagdoun, G. Casano, O. Ouari, M. Schwarzwälder, A.J. Rossini, F. Aussenac, M. Yulikov, G. Jeschke, C. Copéret, A. Lesage, P. Tordo, L. Emsley, Large molecular weight nitroxide biradicals providing efficient dynamic nuclear polarization at temperatures up to 200 K, J. Am. Chem. Soc. 135 (2013) 12790–12797.
[26] T.V. Can, Q.Z. Ni, R.G. Griffin, Mechanisms of dynamic nuclear polarization in insulating solids, J. Magn. Reson. 253 (2015) 23–35.
[27] G. Mathies, M.A. Caporini, V.K. Michaelis, Y. Liu, K.-N. Hu, D. Mance, J.L. Zweier, M. Rosay, M. Baldus, R.G. Griffin, Efficient dynamic nuclear polarization at 800 MHz/527 GHz with trityl-nitroxide biradicals, Angew. Chem. Int. Ed. 54 (2015) 11770–11774.
[28] A.P. Jagtap, M.-A. Geiger, D. Stöppler, M. Orwick-Rydmark, H. Oschkinat, S.Th. Sigurdsson, bcTol: a highly water-soluble biradical for efficient dynamic nuclear polarization of biomolecules, Chem. Commun. 52 (2016) 7020–7023.
[29] D.J. Kubicki, G. Casano, M. Schwarzwälder, S. Abel, C. Sauvee, K. Ganesan, M. Yulikov, A.J. Rossini, C. Coperet, A. Lesage, P. Tordo, O. Ouari, L. Emsley, Rational design of nitroxide biradicals for efficient cross-effect dynamic nuclear polarization, Chem. Sci. 7 (2016) 550–558.
[30] F. Mentink-Vigier, G. Mathies, Y. Liu, A.-L. Barra, M.A. Caporini, D. Lee, S. Hediger, R.G. Griffin, G. de Paëpe, Efficient cross-effect dynamic nuclear polarization without depolarization in high-resolution MAS NMR, Chem. Sci. 8 (2017) 8150–8163.
[31] P. Gast, D. Mance, E. Zurlo, K.L. Ivanov, M. Baldus, M. Huber, A tailored multi-frequency EPR approach to accurately determine the magnetic resonance parameters of dynamic nuclear polarization agents: application to AMUPol, Phys. Chem. Chem. Phys. 19 (2017) 3777–3781.
[32] J. Soetbeer, P. Gast, J. Walish, Y. Zhao, C. George, C. Yang, T.M. Swager, R.G. Griffin, G. Mathies, Conformation of bis-nitroxide polarizing agents by multi-frequency EPR spectroscopy, Phys. Chem. Chem. Phys. 20 (2018) 25506–25517.
[33] D. Wisser, G. Karthikeyan, A. Lund, G. Casano, H. Karoui, M. Yulikov, G. Menzildjian, A.C. Pinon, A. Purea, F. Engelke, S.R. Chaudhari, D. Kubicki, A.J. Rossini, B. Moroz, D. Gajan, C. Coperet, G. Jeschke, M. Lelli, L. Emsley, A. Lesage, O. Ouari, BDPA-nitroxide biradicals tailored for efficient dynamic nuclear polarization enhanced solid-state NMR at magnetic fields up to 21.1 T, J. Am. Chem. Soc. 140 (2018) 13340–13349.
[34] E.A. Nanni, A.B. Barnes, Y. Matsuki, P.P. Woskov, B. Corzilius, R.G. Griffin, R.J. Temkin, Microwave field distribution in a magic angle spinning dynamic nuclear polarization NMR probe, J. Magn. Reson. 210 (2011) 16–23.
[35] E.A. Nanni, A.B. Barnes, R.G. Griffin, R.J. Temkin, THz dynamic nuclear polarization NMR, IEEE Trans THz Sci. Technol. 1 (2011) 1–19.
[36] A.B. Barnes, E. Markhasin, E. Daviso, V.K. Michaelis, E.A. Nanni, S.K. Jawla, E.L. Mena, R. DeRocher, A. Thakkar, P.P. Woskov, J. Herzfeld, R.J. Temkin, R.G. Griffin, Dynamic nuclear polarization at 700 MHz/460 GHz, J. Magn. Reson. 224 (2012) 1–7.
[37] K.R. Thurber, A. Potapov, W.-M. Yau, R. Tycko, Solid-state nuclear magnetic resonance with magic- angle spinning and dynamic nuclear polarization below 25K, J. Magn. Reson. 226 (2012) 100–106.
[38] K.R. Thurber, R. Tycko, Low-temperature dynamic nuclear polarization with helium-cooled samples and nitrogen-driven magic-angle spinning, J. Magn. Reson. 264 (2016) 99–106.
[39] K. Thurber, R. Tycko, Low–temperature dynamic nuclear polarization with helium-cooled samples and nitrogen-driven magic-angle spinning, J. Magn. Reson. 264 (2016) 99–106.
[40] Y. Matsuki, H. Takahashi, K. Ueda, T. Idehara, I. Ogawa, M. Toda, H. Akutsu, T. Fujiwara, Dynamic nuclear polarization experiments at 14.1 T for solid-state NMR, Phys. Chem. Chem. Phys. 12 (2010) 5799–5803.
[41] Y. Matsuki, K. Ueda, T. Idehara, R. Ikeda, I. Ogawa, S. Nakamura, M. Toda, T. Anai, T. Fujiwara, Helium-cooling and –spinning dynamic nuclear polarization for sensitivity-enhanced solid-state NMR at 14 T and 30 K, J. Magn. Reson. 225 (2012) 1–9.
[42] Y. Matsuki, T. Idehara, J. Fukazawa, T. Fujiwara, Advanced instrumentation for DNP-enhanced MAS NMR for higher magnetic fields and lower temperatures, J. Magn. Reson. 264 (2016) 107–115.
[43] Y. Matsuki, S. Nakamura, S. Fukui, H. Suematsu, T. Fujiwara, Closed cycle cold helium magic- angle spinning for sensitivity-enhanced multi-dimensional solid-state NMR, J. Magn. Reson. 259 (2015) 76–81.
[44] E. Bouleau, P. Saint-Bonnet, F. Mentink-Vigier, H. Takahashi, J.-F. Jacquot, M. Bardet, F. Aussenac, A. Purea, F. Engelke, S. Hediger, D. Lee, G. de Paepe, Pushing sensitivity limits using dynamic nuclear polarization with closed-loop cryogenic helium sample spinning, Chem Sci. 6 (2015) 6806–6812.
[45] D. Lee, E. Bouleau, P. Saint-Bonnet, S. Hediger, G. de Paepe, Ultra-low temperature DNP, J. Magn. Reson. 264 (2016) 116–124.
[46] D.E.M. Hoff, B.J. Albert, E.P. Saliba, F.J. Scott, E.J. Choi, M. Mardini, A.B. Barnes, Frequency swept microwaves for hyperfine decoupling and time-domain dynamic nuclear polarization, Sol. State NMR 72 (2015) 79–89.
[47] E.P. Saliba, E.L. Sesti, F.J. Scott, B.J. Albert, E.J. Choi, N. Alaniva, C. Gao, A.B. Barnes, Electron decoupling with dynamic nuclear polarization in rotating solids, J. Am. Chem. Soc. 139 (2017) 6310–6313, https://doi.org/10.1021/jacs.7b02714.
[48] B.J. Albert, S. Ho Pahng, N. Alaniva, E.L. Sesti, P.W. Rand, E.P. Saliba, F.J. Scott, E. J. Choi, A.B. Barnes, Instrumentation for cryogenic magic angle spinning dynamic nuclear polarization using 90 liters of liquid nitrogen per day, J. Magn. Reson. 283 (2017) 71–78, https://doi.org/10.1016/j.jmr.2017.08.014.
[49] F.J. Scott, E.L. Sesti, E.J. Choi, A.J. Laut, J.R. Sirigiri, A.B. Barnes, Magic angle spinning NMR with metallized rotors as cylindrical microwave resonators, Magn. Reson. Chem. 56 (2018) 831–835, https://doi.org/10.1002/mrc.4744.
[50] P. Chen, B.J. Albert, C. Gao, N. Alaniva, L.E. Price, F.J. Scott, E.P. Saliba, E.L. Sesti, P.T. Judge, E.W. Fisher, A.B. Barnes, Magic angle spinning spheres, Sci. Adv. 4 (2018) eaau1540.
[51] A.B. Barnes, "Integrated epr nmr with frequency agile gyrotron", US Patent US10113984B2, 2014.
[52] T. Maly, J. Sirigiri, Sample irradiation techniques for solid-state DNP-NMR spectroscopy, in: 55th ENC, Boston, 2014.
[53] T. Maly, J.R. Sirigiri, Simplified THz instrumentation for high-field DNP-NMR spectroscopy, Appl. Magn. Reson. 43 (2012) 181–194.
[54] J.R. Sirigiri, T. Maly, Integrated high-frequency generator system utilizing the magnetic field of the target application, Patent Application WO2012/096644A1, 2011.
[55] H. Ryan, J. van Bentum, T. Maly, A ferromagnetic shim insert for NMR magnets – towards an integrated gyrotron for DNP-NMR spectroscopy, J. Magn. Reson. 277 (2017) 1–7.
[56] A. Purea, F. Engelke, A. Krahn, Mikrowellen-Einkopplung in MAS-Stator, European Patent EP000003030917B1, 2014.
[57] D. Doty, A tunable microwave resonator for static dynamic nuclear polarization (DNP), Patent application WO 2015/107512 A1, 2014.
[58] A. Krahn, F. Engelke, NMR-Probenkopf mit einem Mikrowellenresonator mit Distributed Bragg Reflector, Patent DE 10 2013 214 930 B4, 2013.
[59] A. Purea, A. von Bieren, MAS-Stator eines NMR-Probenkopfes mit optimierter Mikrowellen- einstrahlung, Patent DE 10 2016 207 998 B3, 2016.
[60] T. Fujiwara, Y. Matsuki, S. Nakamura, NMR-Sonde, Patent Application DE 10 2016 000 863 A1, 2016.
[61] K.J. Pike, T.F. Kemp, H. Takahashi, R. Day, A.P. Howes, E.V. Kryukov, J.F. MacDonald, A.E.C. Collis, D.R. Bolton, R.J. Wylde, M. Orwick, K. Kosuga, A.J. Clark, T. Idehara, A. Watts, G.M. Smith, M.E. Newton, R. Dupree, M.E. Smith, A spectrometer designed for 6.7 and 14.1 T DNP- enhanced solid-state MAS NMR using quasi-optical microwave transmission, J. Magn. Reson. 215 (2012) 1.
[62] M. Rosay, M. Blank, F. Engelke, Instrumentation for solid-state dynamic nuclear polarization with magic angle spinning NMR, J. Magn. Reson. 264 (2016) 88–98.
[63] A.A. Nevzorov, S. Milikisiyants, A.N. Marek, A.I. Smirnov, Multi-resonant photonic band-gap/saddle coil DNP probehead for static solid-state NMR of microliter volume samples, J. Magn. Reson. 297 (2018) 113–123.
[64] A. Macor, E. de Rijk, G. Annino, Over-moded resonant cavity for magnetic resonance based on a photonic band gap structure, Patent application 2012 WO2013/057688 A1, 2011.
[65] G. Annino, A. Macor, E. deRijk, S. Alberti, Magnetic resonance hyperpolarization probe head, Patent application, WO 2013 000508 A1, 2011.
[66] A. Macor, E. deRijk, G. Annino, S. Alberti, J.-Ph Ansermet, THz-waves channeling in a monolithic saddle coil for dynamic nuclear polarization enhanced NMR, J. Magn. Reson. 212 (2011) 440–449.
[67] T. Dubroca, A.N. Smith, K.J. Pike, S. Froud, R. Wylde, B. Trociewitz, J. McKay, F. Mentink-Vigier, H. van Tol, S. Wi, W. Brey, J.R. Long, L. Frydman, S. Hill, A quasioptical and corrugated microwave transmission system for simultaneous dynamic nuclear polarization NMR on two separate 14.1 T spectrometers, J. Magn. Reson. 289 (2018) 34–44.
[68] A. Lund, I. Kaminker, S. Jain, K. Tagami, S. Han, Method and hardware optimization for MAS DNP at 25 K, in: 58th ENC, Asilomar, 2017.
[69] F. Engelke, A. Purea, C. Reiter, F. Aussenac, Sub-THz technology for dynamic nuclear polarization in nuclear magnetic resonance (DNP NMR): transverse confinement of microwave propagation through heterogeneous solid DNP samples, Europ. Phys. J. (EPJ Web of Conferences) 149 (2017) 01009.
[70] A. Purea, C. Reiter, A. Dimitriades, NMR-MAS-Probenkopf mit optimiertem MAS-DNP- Spulenklotz für schnelle Probenrotation, Patent application DE102018204913, 29 March 2018.
[71] A. Purea, B. Ell, C. Reiter, F. Aussenac, F. Engelke, Augmenting microwave irradiation in MAS DNP samples at 263 GHz, Europ. Phys. J. (EPJ Web of Conferences) 187 (2018) 01005.
[72] A.K. Klein, J. Hammler, C. Balocco, A.J. Gallant, Machinable ceramic for high performance and compact THz optical components, Opt. Mater. Express 8 (2018) 1968–1975.
[73] I.V. Sergeyev, F. Aussenac, A. Purea, C. Reiter, E. Bryerton, S. Retzloff, J. Hesler, L. Tometich, M. Rosay, Efficient 263 GHz magic angle spinning DNP at 100K using solid-state diode sources, submitted to Solid-State NMR 2019.
[74] K.R. Thurber, R. Tycko, Measurement of sample temperatures under magicangle spinning from the chemical shift and spin–lattice relaxation rate of 79Br in KBr powder, J. Magn. Reson. 196 (2009) 84–87.
[75] A. Purea, B. Ell, F. Aussenac, C. Reiter, I.P. Pagonakis, A. Dimitriades, E. de Rijk, F. Engelke, Global and local characterization of microwave fields in homogeneous and heterogeneous solid-state MAS DNP NMR samples (in preparation).
[76] K.R. Thurber, W.-M. Yau, R. Tycko, Low-temperature dynamic nuclear polarization at 9.4 T with a 30 mW microwave source, J. Magn. Reson. 204 (2010) 303–313.

[77] A. Henstra, P. Dirksen, J. Schmidt, W.T. Wenckebach, Nuclear spin orientation via electron spin locking (NOVEL), J. Magn. Reson. 77 (1988) 389–393.
[78] T.V. Can, J.J. Walish, T.M. Swager, R.G. Griffin, Time domain DNP with the NOVEL sequence, J. Chem. Phys. 143 (2015) 054201.
[79] G. Mathies, S. Jain, M. Reese, R.G. Griffin, Pulsed dynamic nuclear polarization with trityl radicals, J. Phys. Chem. Lett. 7 (2016) 111–116.
[80] T.V. Can, R.T. Weber, J.J. Walish, T.M. Swager, R.G. Griffin, N.O.V.E.L. Ramped-amplitude, J. Chem. Phys. 146 (2017) 154204.
[81] S.K. Jain, G. Mathies, R.G. Griffin, Off-resonance NOVEL, J. Chem. Phys. 147 (2017) 164201.
[82] T.V. Can, R.T. Weber, J.J. Walish, T.M. Swager, R.G. Griffin, Frequency-swept integrated solid effect, Angew. Chem. Int. Ed. 56 (2017) 1–6.
[83] T.V. Can, R.T. Weber, J.J. Walish, T.M. Swager, R.G. Griffin, Frequency-swept integrated solid effect, Angew. Chem. Int. Ed. 65 (2017) 6744–6748.
[84] R. Annabestani, M.S. Mirkamali, R. Budakian, Adiabatic NOVEL for nano-scale magnetic resonance imaging, arXiv:1712.09128v1 [quant-ph] 25 Dec 2017.
[85] T.V. Can, J.E. McKay, R.T. Weber, C. Yang, T. Dubroca, J. van Tol, S. Hill, R.G. Griffin, Frequency-swept integrated stretched solid effect dynamic nuclear polarization, J. Phys. Chem. Lett. 9 (2018) 3187–3192.
[86] K.O. Tan, C. Yang, R.T. Weber, G. Mathies, R.G. Griffin, Time-optimized pulsed dynamic nuclear polarization, Sci. Adv. 5 (2019) eaav6909.
[87] E.A. Nanni, S. Jawla, S.M. Lewis, M.A. Shapiro, R.J. Temkin, Photonic-band-gap gyrotron amplifier with picosecond pulses, Appl. Phys. Lett. 111 (2017) 233504.
[88] E.A. Nanni, S.M. Lewis, M.A. Shapiro, R.G. Griffin, R.J. Temkin, Photonic-band-gap traveling- wave gyrotron amplifier, Phys. Rev. Lett. 111 (2013) 235101.
[89] B. Corzilius, A.A. Smith, R.G. Griffin, Solid effect in magic angle spinning dynamic polarization, J. Chem. Phys. 137 (2012) 054201.
[90] T.V. Can, M.A. Caporini, F. Mentink-Vigier, B. Corzilius, J.J. Walish, M. Rosay, W. E. Maas, M. Baldus, S. Vega, T.M. Swager, R.G. Griffin, Overhauser effect in insulating solids, J. Chem. Phys. 141 (2014) 064202.
[91] A.S.L. Thankamony, J.J. Wittmann, M. Kaushik, B. Corzilius, Dynamic nuclear polarization for sensitivity enhancement in modern solid-state NMR, Prog. NMR Spectrosc. 102–103 (2017) 120–195.
[92] D.J. Kubicki, A.J. Rossini, A. Purea, A. Zagdoun, O. Ouari, P. Tordo, F. Engelke, A. Lesage, L. Emsley, Amplifying dynamic nuclear polarization of frozen solutions by incorporating dielectric particles, J. Am. Chem. Soc. 136 (2014) 15711–15718.